HHS Public Access

Author manuscript

NMR Biomed. Author manuscript; available in PMC 2021 April 01.

Published in final edited form as:

NMR Biomed. 2020 April ; 33(4): e4216. doi:10.1002/nbm.4216.

Longitudinal Assessment of Recovery after Spinal Cord Injury with Behavioral Measures and Diffusion, Quantitative Magnetization Transfer and Functional MRI

Tung-Lin Wu[1,2,*], **Nellie E. Byun**[1,3], **Feng Wang**[1,3], **Arabinda Mishra**[1,3], **Vaibhav A. Janve**[1,3], **Li Min Chen**[1,3], **John C. Gore**[1,2,3,4,5]

[1]Vanderbilt University Institute of Imaging Science, Nashville, TN, 37232, United States

[2]Biomedical Engineering, Vanderbilt University, Nashville, TN, 37232, United States

[3]Radiology and Radiological Sciences, Vanderbilt University Medical Center, Nashville, TN, 37232, United States

[4]Physics and Astronomy, Vanderbilt University, Nashville, TN, 37232, United States

[5]Molecular Physiology and Biophysics, Vanderbilt University, Nashville, TN, 37232, United States

Abstract

Spinal cord injuries (SCIs) are a leading cause of disability and can severely impact the quality of life. However, to date, the processes of spontaneous repair of damaged spinal cord remain incompletely understood, partly due to a lack of appropriate longitudinal tracking methods. Non-invasive, multi-parametric magnetic resonance imaging (MRI) provides potential biomarkers for the comprehensive evaluation of spontaneous repair after SCI. In this study in rats, a clinically relevant contusion injury was introduced at the lumbar level that impairs both hindlimb motor and sensory functions. Quantitative MRI measurements were acquired at baseline and serially post-SCI for up to two weeks. The progressions of injury and spontaneous recovery in both white and gray matter were tracked longitudinally using pool-size ratio (PSR) measurements derived from quantitative magnetization transfer (qMT) methods, measurements of water diffusion parameters using diffusion tensor imaging (DTI), and intra-segment functional connectivity derived from resting state functional MRI. Changes in these quantitative imaging measurements were correlated with behavioral readouts. We found (1) a progressive decrease in PSR values within two weeks post-SCI, indicating a progressive demyelination at the center of the injury that was validated with histological staining; (2) PSR correlated closely with fractional anisotropy and transverse relaxation of free water, but did not show significant correlations with behavioral recovery; (3) preliminary evidence that SCI induced a decrease in functional connectivity between dorsal horns below the injury site at 24 hours. Findings from this study not only confirm the value of qMT and DTI methods for assessing the myelination state of injured spinal cord but indicate that they may also have further implications on whether therapies targeted towards remyelination may be appropriate. Additionally, a better understanding of changes after SCI provides valuable information to guide and assess interventions.

[*]Corresponding author at: Vanderbilt University Institute of Imaging Science, 1161 21st Avenue South, MCN B0104, Nashville, TN, 37232. tung-lin.wu@vanderbilt.edu.

Graphical Abstract

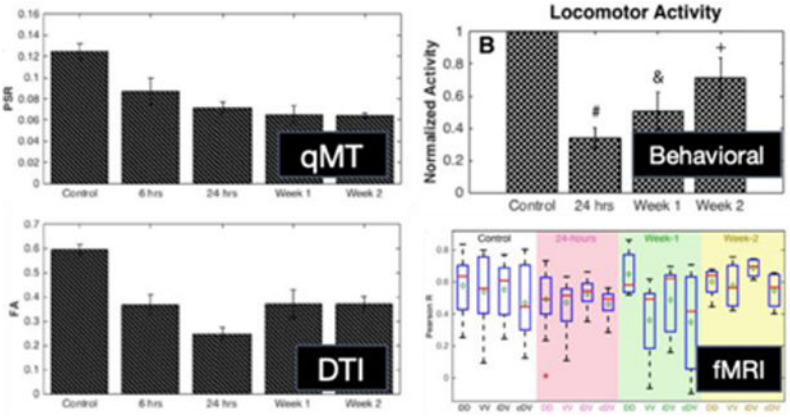

To date, the processes of spontaneous repair of damaged spinal cord remain incompletely understood, partly due to a lack of appropriate tracking methods. Non-invasive multi-parametric magnetic resonance imaging (MRI) provides potential biomarkers for comprehensive evaluation of spontaneous repair after spinal cord injuries. In this study, we found the use of longitudinal *in vivo* quantitative magnetization transfer, functional MRI and diffusion tensor imaging along with behavioral and histological assessments provide complementary information about the progression after spinal cord injuries.

Keywords

diffusion MRI; functional MRI; magnetization transfer; spinal cord injury; myelination

INTRODUCTION

Spinal cord injuries (SCIs) are a leading cause of disability and can lead to devastating consequences for patients. To date, complete restorative therapies for SCIs have yet to be devised, and although damaged cords may repair spontaneously, the underlying mechanisms involved remain poorly understood, partly due to a lack of appropriate longitudinal monitoring methods. The initial physical impact of a SCI damages spinal tissues by eliciting vascular responses, edema, and neuronal death that disrupt conduction in white matter tracts and gray matter function (1). Subsequently, the initial damage triggers a cascade of pathological events, termed secondary injury. While the initial injury is irreversible as it occurs in seconds to minutes, minimizing secondary injury is the primary goal for immediate medical interventions during the acute injury phase (<24 hours post injury). Over time, intrinsic repair processes involving the formation of glial scars made up of reactive astrocytes (2), loss of oligodendrocytes (3,4), as well as inflammatory responses mediated by microglia and macrophages (5,6), may be initiated. Given the complex dynamics of the multifaceted processes that arise after traumatic injury, the development of non-invasive imaging biomarkers that provide a comprehensive assessment of the spontaneous repair and functional changes that occur within spinal cord could be critical for determining the optimal time window, targets and effectiveness of therapeutic interventions.

Quantitative multi-parametric MRI presents an attractive technique for revealing changes in composition, microstructure, and function of the spine non-invasively. For example, diffusion tensor imaging (DTI) exploits anisotropy of water motion in white matter fibers (7,8), and has previously been used to provide microstructural information about the white matter and its fiber organization in both the brain and spinal cord. Variations in indices such as axial (AD) and radial diffusivity (RD) values have previously been shown to reflect axonal damage and demyelination, respectively. Similarly, fractional anisotropy (FA) and apparent diffusion coefficient (ADC) encompass broader information on microstructure including cell density, axonal density, fiber coherence, and myelination status (9). Importantly, previous studies have also demonstrated that DTI can successfully predict various grades of injury severity at different time points (10,11).

A second quantitative MR method potentially capable of tracking SCI associated tissue property changes is magnetization transfer (MT) imaging. MT exploits interactions between immobile macromolecular and free water protons, including chemical exchange and dipole-dipole couplings, to indirectly measure immobile proton content (12). In white matter, significant MT contributions come from myelin, and these have been shown in several studies to reveal demyelination under different pathological conditions that have been confirmed with histology (13,14). While images with contrast that reflect MT effects can be described semi-quantitatively in terms of an MT ratio (MTR), this is non-specific and depends on various non-MT factors (15). Alternatively, more elaborate imaging protocols can be analyzed in terms of a model of tissue to produce quantitative measurements of specific intrinsic MT parameters. In particular, quantitative MT (qMT) provides measurements of the pool size ratio (PSR, the ratio of the free water and immobile macromolecular pools) isolated from the effects of relaxation and exchange rates (15,16), and is a more specific indicator of myelination in white matter tracts.

A contusion injury to spinal cord drastically disrupts both tissue structure and cord functions concurrently. While DTI and qMT convey information about tissue composition and structure, they do not reflect cord functions. The functional integrity of spinal gray matter circuits can be evaluated non-invasively with functional MRI (fMRI). FMRI detects blood oxygenation level dependent (BOLD) contrast and has been extensively applied to study the functional organization of the brain as well as functional connectivity between regions using resting state fMRI (rsfMRI) (17,18). Recently, resting-state fMRI has been exploited successfully to reveal functional connectivity between spinal horns in awake humans (19) and in anesthetized monkeys and rats (20,21), despite the challenges created by the small size of the cord and the presence of physiological noise. The translation of rsfMRI to monitor functional changes within intraspinal circuits after SCI provides complementary information to DTI and qMT methods.

Dorsal column lesion models have been shown to be well-suited for studying neuron-intrinsic regenerative responses (22). We previously reported the use of diffusion, fMRI, and qMT imaging to study plastic changes over a period of months in the spinal cord of non-human primates that underwent a unilateral dorsal column transection injury of the cervical spinal cord (23,24). However, contusion injuries to thoracic and/or lumbar regions are more relevant to those that present clinically in human subjects. Thus, the primary objectives of

the current study were to (1) characterize and monitor structural and functional changes in the lumbar spinal cord following a contusion injury in rats, and (2) relate these changes in the spinal cord to behavioral performance. In this study, multi-parametric MRI acquisitions (DTI, qMT, and fMRI) were acquired from healthy rats as well as from rats that underwent a moderate contusion injury at the lumbar L2 level. The progression and recovery of the injury in white matter tracts were tracked longitudinally with DTI and qMT, while behavioral assessments and histological data after staining for myelin were collected in parallel at different time points for up to 2 weeks post-injury. In addition, the functional integrity of intraspinal circuits was assessed by computing functional connectivity changes below the injury site post injury in a subset of animals. We present evidence that multi-parametric MRI is capable of detecting and monitoring functionally-relevant pathological changes that occur in both grey and white matter. An improved understanding of the spontaneous repair processes of spinal cord should be informative for designing effective therapeutic interventions and for evaluating treatment outcomes in rodent models of SCI.

METHODS

Animals

A total of 26 adult male Sprague Dawley rats (Envigo, formerly Harlan) were included in this study. Animals were housed in a vivarium maintained at 22 degrees Celsius on a 12 h light/dark cycle with food and water provided *ad libitum*. Rats were initially housed in groups of 2–3 per cage and after spinal cord injury were single housed. All experiments were authorized by the Vanderbilt University Institutional Animal Care and Use Committee and conform to all NIH/PHS guidelines for use of animals in research.

Animal spinal cord injury

A subset of rats (n=16) underwent SCI. Each animal was initially anesthetized with 2.5% isoflurane before a midline sagittal incision of ~5 cm was made over the lumbar vertebrae, and muscle and connective tissues were separated and retracted from the vertebrae to expose the underlying vertebral spinal column segments. A dorsal laminectomy was then performed using a fine tipped rongeur for removing vertebral processes. A typical opening measured up to 3 mm^2 of the spinal cord, larger than the 2.5 mm diameter of the impactor tip. The Infinite Horizon Impactor – a device designed for the application of standard force injuries to the spinal cords of rodents – was used in this study. Within the exposed spinal cord, two Adson forceps were used to clamp and rigidly secure the vertebral spinal column by securing the transverse processes of the vertebral spinal column approximately 1 mm rostral and caudal to the laminectomy. The impact was initiated at a moderate injury level (160 kDynes) at the upper L2 segment. Post-operative wound closure was completed by apposing and suturing the dissected muscle. Post-operative care included the administration of analgesics (carprofen 5–15 mg/kg, s.c.). The bladder was manually expressed as needed.

Animal imaging preparation

After injury, rats were imaged at different time points (at 6 hours, 24 hours, 1 week, and 2 weeks) post-injury. For practical reasons, not all animals received MRI scanning on every time point; Table S1 presents a log of MRI data collected for each rat. Before MRI scans,

animals were first anesthetized with 3% isoflurane and then underwent endotracheal intubation followed by mechanical ventilation (70–75 breaths/min ventilation rate). After the animal stabilized, respiration rate was adjusted to 60–66 breaths/min for the scans. Vital signs were continuously monitored throughout each session, and included respiration using a pneumatic pillow, rectal temperature and end-tidal CO_2. Respiratory traces were also recorded and later used in fMRI data preprocessing to correct their effects on BOLD signals. Animals were then placed on a customized bed in the supine position with an elastic medical tape tightened around the animal and coil. A minimum of one hour was allocated for each animal to stabilize physiologically, during which shimming (automatic global shimming followed by local shimming over the spinal cord) was performed, followed by power calibration on a single coronal slice covering the dorsal column. Subsequently, anatomical, DTI, qMT and rsfMRI images were acquired.

Image Acquisition

MR images were acquired on a 9.4T Varian magnet with a 2-cm diameter transmit-receive radio frequency coil. Anatomical images were acquired with MT contrast (MTC) on three planes that accentuates the grey-white matter boundaries. Specifically, the pulse sequence uses a gradient echo acquisition with a Gaussian saturation pulse (flip angle of 820° and offset 5000Hz from water) with the following acquisition parameters: TR/TE=200/3ms, matrix size=128×128, FOV=32×32 mm^2, in-plane resolution=250×250 μm^2, slice thickness = 3000 μm (axial), 500 μm (coronal) and 750 μm (sagittal), flip angle=35°). Figure 1A presents a high-resolution axial image referenced for coronal slice selection (red dashed lines) that includes the dorsal column for quantitative MRI imaging.

Diffusion weighted images were acquired using a respiratory-gated pulsed gradient spin-echo EPI imaging sequence with the following acquisition parameters: TR/TE=2000/27.61ms, number of excitations (NEX)=8, voxel size=333×333×700μm^3, 12 directions, b-values of 0 and 1000 s/mm^2, diffusion gradient amplitude=28.13 G/cm, duration=4.00ms, separation=12ms. Five coronal slices were imaged with the second slice covering the posterior position of the spinal cord with the dorsal column and dorsal horns.

QMT images were acquired with the following parameters: TR/TE=28/2.97ms, NEX=32, voxel size=250×250×700 μm^3 in the same acquisition plane as the second slice of DTI. Slice-selective Gaussian-shaped saturation pulses at two different powers were applied (flip angle=220° and 820°) with eight different frequency offsets ranging from 1000 Hz to 80000 Hz at constant logarithmic interval with an additional data point acquired at 6000 Hz. A 10ms saturation pulse was used. The continuous wave power approximation (ω_{1CWPE}) for Gaussian-shaped saturation pulses was used to obtain flip angles 220° and 820° (pulse amplitudes 301.26 rad/s (1.13 μT) and 1122.89 rad/s (4.20 μT) respectively). While previous brain imaging studies have suggested acquiring less data points (fewer RF offsets) may be sufficient (24–26), the larger motion artifacts in the spinal cord required additional data points for accurate pixel-by-pixel fitting. T_1 maps were also acquired to obtain averaged observed relaxation rate R_{1obs} in healthy controls using an inversion recovery sequence (Supplementary Figure S1). Longitudinally, DTI and qMT scans were performed at 6 hrs, 24 hrs, week-1 and week-2 post-SCI.

Resting-state fMRI data of the lumbar spinal cord were acquired with a similar protocol as our previous publication (21) using multishot gradient echo planar images with TR/TE=500/6.70ms, 6 shots, resolution=330×330×3000 μm^3, 180 volumes, five slices in the axial plane. The relatively short echo time was selected to reduce distortions and signal losses caused by field inhomogeneities while still preserving sensitivity to BOLD effects at 9.4T.

MRI data analyses

QMT: MRI data analyses were performed using MATLAB. Similar to our previous publication (24), qMT data were fitted using the Henkelman-Ramani two-pool model (27). MT-weighted MR signals collected were expressed as a function of irradiation amplitudes of continuous wave power equivalent (ω_{CWPE}), which is proportional to the square of the flip angles (θ_{sat}) of the saturation pulse, and at multiple frequency offsets (Δf) using:

$$S(\omega_{CWPE},\Delta f) = \frac{M_0\left(R_{1b}\left[\frac{RM_{0b}}{R_{1a}}\right]+R_{RFB}(\omega_{1CWPE},\Delta f,T_{2b})+R_{1b}+\frac{RM_{0b}}{F}\right)}{\left[\frac{RM_{0b}}{R_{1a}}\right](R_{1b}+R_{RFB}(\omega_{1CWPE},\Delta f,T_{2b}))+\left(1+\left[\frac{\omega_{CWPE}}{2\pi\Delta f}\right]^2\left[\frac{1}{T_{2a}R_{1a}}\right]\right)\left(R_{RFB}(\omega_{1CWPE},\Delta f,T_{2b})+R_{1b}+\frac{RM_{0b}}{F}\right)} \quad (1)$$

Subscripts a and b in Equation 1 (25,28) denote free water and macromolecular protons respectively. F, also known as the pool size ratio (PSR), represents the ratio of free water and macromolecular pool (M_{0b}/M_{0a}) and has been reported to be correlated with myelin content in white matter; M_{0a} and M_{0b} represent the fully relaxed values of magnetization in their respective pools. In addition, M_0 is the magnetization signal without MT contrast while R_{RFB} is the rate of saturation of the macromolecular pool and is dependent on ω_{CWPE}, Δf, and transverse relaxation T_{2b}. Conventional notations of R_{1a} ($1/T_{1a}$) and R_{1b} ($1/T_{1b}$) are the longitudinal relaxation rates for protons in the respective proton pools. Because estimates of the other fitted parameters are largely insensitive to the value of R_b, it was also set as a constant at $1s^{-1}$ (26,28,29). On the other hand, R_{1a} is dependent on the observed longitudinal relaxation rate (R_{1obs}) and was included in the model as Equation 2 (25,28):

$$R_{1a} = R_{1obs} - \frac{RM_{0b}(R_{1b}-R_{1obs})}{R_{1b}-R_{1obs}+\frac{RM_{0b}}{F}} \quad (2)$$

With qMT data fitted to the above model, five parameters were estimated for each pixel: M_0, F, RM_{0b} T_{2a} and T_{2b}. Figure 1F presents an example of the fitted model to normalized signals obtained from a selected white matter voxel in the spinal cord at two saturation powers and multiple frequency offsets. Performance of the model fitting was also estimated by assessing the least squares of the residuals. Fitted data pixels with residuals greater than 0.01 were excluded from further analysis. Lastly, effects of B_1 and B_0 inhomogeneities on PSR maps were evaluated (Supplementary Figures S2-S4) and appeared to have minimal effects on the overall trends observed.

DTI: The diffusion data were fitted to mono-exponential decays as a function of gradient b values, and the resultant set of diffusion coefficients were fitted to a symmetric 3×3 tensor from which ADC, AD, RD, and FA for each voxel were estimated.

Pearson's correlation coefficients were computed in the region of interest (ROI) at the epicenter of the injury between PSR and other fitted PSR parameters – R_{2a}, R_{2b} and RM_{0b}, as well as diffusion metrics, on a run-by-run basis. Similarly, behavioral assessments (see below), and histological myelin stained sections (see below) were correlated with PSR using the average value at each time point post-SCI. Statistical comparisons of PSR and MTR values between different time points were also performed using non-parametric Wilcoxon rank sum tests corrected for false discovery rate (FDR) to determine whether groups of measurements at different time points were significantly different from each other.

FMRI: Data pre-processing and ROI analyses of spinal rsfMRI data were similar to our previous publications (20,21,30). Briefly, fMRI images were pre-processed with slice-by-slice rigid body motion corrections with three motion parameters before they were up-sampled to 250×250×3000 μm^3. Manual alignments were subsequently performed between the fMRI and corresponding anatomical images. "Nuisance" signals were then derived from muscle, white matter, cerebrospinal fluid and surgifoam voxels using principal component analysis. The first three to five signal components that accounted for at least 70% of the cumulative signal variance along with motion correction parameters were used as signal regressors in a general linear model to reduce their effects on the BOLD time series. The fMRI data were then bandpass filtered with a pass-band between 0.01 and 0.1Hz using a Chebyshev Type II filter (18). Runs with x-y translations greater than 5 voxels were excluded. Additionally, runs in control (baseline) rats with tSNR less than 50 in the spinal horns were removed. For ROI analysis, m individual voxel time series of a spinal horn were correlated with n time series of another spinal horn. The maximum of this correlation vector was then extracted as the functional connectivity metric between the pair of horns. This was performed for all pairs of ROIs.

Histological Staining

At different time points after SCI, a subset of rats were euthanized with an overdose of isoflurane and transcardially perfused with PBS/saline solution followed by 10% buffered formalin phosphate fixative. The spinal cords were excised and soaked overnight in formalin phosphate before wax embedding for sectioning. Histological staining with Luxol Fast Blue (LFB) of the post-mortem tissue slices was then performed to evaluate the degree and extent of demyelination due to the contusion injury. Sections 10 μm thick were first sliced in the coronal orientation, de-waxed and cleared in 95% ethanol, and stained in LFB solution overnight at 56–58 degrees Celsius. Sections were then rinsed in 95% alcohol to remove excess stain before rinsing with distilled water. To differentiate gray versus white matter, slides were immersed in lithium carbonate solution for 10 seconds and then placed in 70% ethanol until gray matter and white matter were distinguishable. Finally, high-resolution imaging of whole slides (25 mm × 75 mm standard microscope slides) in brightfield were imaged on a Leica SCN400 Slide Scanner (Leica Biosystems). Tissues were originally imaged at 20X magnification to a resolution of 0.5 μm/pixel. For microscopy, optical

intensity changes on myelin stains at the center of the injury (mean ROI size = 3.28mm^2) were quantitatively evaluated; the degree of de-myelination was assessed by the percentage decrease of the regional intensity relative to control regions on the same slice similar to procedures described in Janve et al. (31).

Behavioral assessments

Baseline and post-SCI behavioral readouts were assessed, specifically locomotor activity, Von Frey thresholds, and hot plate response latencies (see a review (30)). Before behavioral testing, rats were first habituated for at least 45 minutes in the testing room. For locomotor activity, each rat was placed into separate open field chambers equipped with x- and y-axis infrared beams (MedAssociates, St. Albans, VT), and spontaneous motor activity was assessed for 30 minutes. Beam breaks were recorded as measurements of horizontal movement.

Von Frey filaments were used to measure the mechanical sensitivity of both hind paws. Each rat was placed on a mesh wire floor with plastic cover and allowed to habituate for 30–45 minutes. Von Frey monofilaments of various strengths (2g, 4g, 6g, 8g, 10g and 15g) were manually applied perpendicular to the hind paw. A positive response was recorded if the rat withdrew, licked, or shook the stimulated paw either during or immediately after the application of the filament. If the rat did not respond after 10 applications, this was recorded as no response. For rats with SCI, filaments with strength up to 26g were also applied, and if unresponsive 10 times, the filament strength at 78g was recorded as the threshold. For SCI rats that dragged their hind limbs, the animal was tested in its home cage with corncob bedding (no mesh wire bottom) as the foot was prone. Locomotor and Von Frey assays were performed at baseline, then post-injury at 24 h, 1-week, and 2-week time points.

Finally, nociception was assessed using the hot plate test at 55 degrees Celsius (Columbus Instruments, Columbus, OH). Latency to withdraw, lick, or shake a hind paw were recorded and indicated a nociceptive response. If unresponsive by 15 seconds, the rat was removed to prevent injury. Hot plate tests were performed at baseline, week-1 and week-2 time points; the 24-h time point was not assessed due to required analgesic administration post-SCI that would confound results.

RESULTS

PSR and FA Revealed Changes at the Injury Site in the Lumbar Spinal Cord

In healthy control rats, MTC images showed significant contrast between white and gray matter of the spinal cord, with gray matter appearing brighter than white matter (Figure 1A-C). PSR maps showed significantly greater values (p=0.0022, Wilcoxon rank sum test) in white matter (mean ± standard error of mean): 0.1247±0.0074) than in gray matter (0.0865 ± 0.0044). These spinal qMT *in vivo* PSR measurements are comparable in range to those obtained in white matter and gray matter of the brain (25,33) and in the cervical spinal cord of NHPs (24). FA values in gray matter were lower than those in white matter, and post-SCI both PSR and FA maps showed lesion related reductions at and near the epicenter of injury (Figure 2). QMT spectra obtained at two flip angles, which were normalized to signal

intensities at 80 kHz offset, are displayed in Figure 2C. Compared to healthy control animals as shown in Figure 1, the qMT post-lesion PSR map identified a low PSR region (Figure 2A, indicated by the red arrows), which was reflected in parallel in the corresponding FA maps (Figure 2B).

Longitudinal PSR changes following injury and correlations with other MR metrics

Changes of PSR and FA at the epicenter of the injury at different time points post-injury, averaged over multiple runs at each time point, are shown in Figure 3. PSR and FA values dropped markedly at 6 hours post-injury and remained low to the end of 2 weeks. At 24-hours post-SCI, PSR was reduced significantly to 57% of control (baseline) values and remained low beyond 24 hours ($p<0.05$, FDR corrected) and continued to diminish over time, in an overall decreasing trend. Consistent with this phenomenon, MTR measurements (Figure 4) of rats throughout the two weeks continued to get progressively lower. FA measurements significantly decreased at 6 hours and reached their lowest values at 24 hours post injury. However, signs of recovery were evident at week-1 and week-2 with increased FA values, although care must be taken with such interpretation given the gradual clearance of edema and inflammation after the first week (see discussion in *Limitations of the Current Study and Future Directions*). FA changes between different time points such as between 6 and 24 hours were also detected (left panel in Figure 3B). In order to understand the relationship between PSR and other MR metrics sensitive to demyelination and macromolecular content, Pearson's correlations were computed between them for both control and SCI rats. QMT parameters including relaxation rates of both pools and exchange rate as well as DTI derived metrics – FA, ADC, AD, and RD – for control and injured animals were plotted as a function of PSR in Figure 5. Distinct clusters were noticeable between controls and injured groups in all plots. Quantitatively, FA ($r=0.64$, $p=2.78\times10^{-5}$) and R_{2a} ($r=0.68$, $p=2.96\times10^{-6}$) showed significant positive correlations while ADC ($r=-0.07$, $p=0.68$) and AD ($r=0.16$, $p=0.36$) were most weakly coupled with PSR as shown in Figure 5H.

Relationship between PSR, FA and behavioral assessments

Longitudinal changes of PSR also correlated with behavioral data (Figure 6). For both Von Frey and locomotor activity evaluations, the greatest deficits were observed at 24 hours post-SCI. Von Frey tests showed that rats were largely unresponsive to filament strengths up to 26g while open-field tests showed a drop in locomotor activity to 34% of baseline. At weeks 1 and 2, however, increasing mechanical sensitivity (reduced mechanical withdrawal thresholds) and locomotion suggest progressive functional recoveries occurred that are further supported by weaker statistical differences from controls as a function of time. Tactile threshold and locomotor activity did not return to control levels at the completion of testing at week 2 post injury. Similarly, hot plate assay results showed impaired nociception at week-1 with a greater latency response time, but a close to full recovery was evident at week-2. Comparisons of behavioral measurements with the decreasing PSR trend, however, showed insignificant correlations (Supplementary Figure S5): $r_{vonfrey\text{-}PSR} = -0.62$ ($p=0.38$), $r_{locomotor\text{-}PSR} = 0.79$ ($p=0.21$), and $r_{hotplate\text{-}PSR} = -0.57$ ($p=0.61$). On the other hand, correspondences between FA and behavioral measurements demonstrated greater

correlations as signs of recovery or increased FA were present at week-1 and week-2: $r_{vonfrey\text{-}FA} = -0.89$ (p=0.11), $r_{locomotor\text{-}FA} = 0.95$ (p=0.05), and $r_{hot\ plate\text{-}FA} = -0.59$ (p=0.60).

Validation of PSR and FA with histology

LFB was used to stain for myelin and validate measurements obtained from PSR maps. Figure 7 presents LFB stained sections at the dorsal column from rats obtained at baseline, 24-hours, week-1, and week-2 post-SCI. Continuous and distinct white and gray matter strips (yellow and purple arrows) are evident with high intensity stains mostly restricted to white matter (yellow arrows). Intensity of LFB staining at the center of injury was reduced with more granular patches visible (reduced to 45.61±0.07% of controls) at 24 hours post SCI. Consistent with the PSR trend, intensity of LFB stains at the epicenter was further reduced to 28.21±0.01% at week 1 post SCI and 23.27±0.02% of controls at week 2 post SCI. Correlation of the time course of LFB measurements with PSR (r=0.99, p=0.01) was significantly greater than that with FA (r=0.78, p=0.22).

Quantitative changes in inter-horn resting state functional connectivity (rsFC) post-SCI

Axial resting state functional images at the lumbar level were able to distinguish between gray and white matter. In addition, BOLD and MTC anatomical images appear to be well-aligned, indicated by a green cross hair pointing to the left dorsal horn on both images at the same position (Figure 8A-B). Figure 8C, D, F, G present averaged time series of signals from the four horns showing fluctuations similar to those observed at the cervical spinal cord of humans, NHPs, and rats.

Subsequently, we measured changes in inter-horn rsFC at different time points after a contusion injury in a subset of animals. Within-slice resting-state correlation strengths between different seed horn pairs were calculated and averaged for each group (Figure 9). In normal control spinal cords, robust correlations were observed between left and right dorsal horns (mean correlation value of 0.58) as well as dorsal to ipsilateral and contralateral ventral horns (mean correlation values of 0.55 and 0.47, respectively) and between ventral horns (mean correlation value of 0.54). After injury, a notable overall decrease in correlation values was observed at 24 hours in the slice below the injury site. In particular, averaged dorsal-dorsal connectivity strengths decreased by around 15%. At week-1 post-SCI, connectivity between left and right dorsal horns was elevated while by week-2 post-SCI, functional connectivity between dorsal horns appears to return to levels similar to those from controls. However, it is important to note that week-1 and week-2 boxplots consist of a total of five and four runs from two and one animal respectively, and that a much larger number of rats is needed to draw any further robust conclusions. Lastly, correlations between averages of dorsal-dorsal connectivity at different time points with locomotor, Von-Frey and hot plate assessments were found to be 0.33 (p=0.67), −0.49 (p=0.51), and 0.98 (p=0.13)

DISCUSSION AND CONCLUSIONS

PSR as a biomarker for demyelination

In this study, we observed a decreasing trend of PSR starting at 6 hours and continuing throughout two weeks post-SCI, which was later validated with histological results.

Evidences from animal models (34–36) and human specimens (37–39) corroborate the observation that demyelination occurs after SCI, particularly during the acute and subacute phase (40). For example, one of the earliest studies found using electron microscopy that demyelination occurred by 21 hours and continued to worsen within the first week post injury (41). More recently, Ek et al. have also studied pathological changes in white matter following a contusion injury using immunohistochemistry and LFB stains. They reported that the number of myelinated axons decreased to approximately 24% of controls 24 hours post-SCI and by week 1, only 13% remained (42). These results are largely consistent with PSR measurements in this study, suggesting qMT parameters are capable of reflecting specific information about changes in composition and the progression of demyelination at acute stages of SCI.

Relationship between behavioral and demyelination

The behavioral assessments of locomotor activity, mechanosensitivity and nociceptive heat pain thresholds did not show significant correlations with longitudinal PSR measurements. PSR values at the injury epicenter remained low while locomotor and sensory functions showed recovery over the two weeks examined. Re-myelination has been shown to be a spontaneous process where oligodendrocytes and Schwann cells regenerate damaged or lost myelin in the absence of any therapeutic intervention (43,44). Our cross-sectional LFB measurement at the epicenter did not show corresponding increases, suggesting that significant remyelination did not occur, so that behavioral improvements are unlikely to be mediated through myelination changes of the tissue at the injury center.

Previous studies have found correlations between re-myelination and behavioral recovery in animal models with non-injury type demyelination (see a review (43)). Duncan et al. reported re-myelination along the entire spinal cord was accompanied with improvements in locomotion at least 6 months after demyelination was introduced by feeding animals an irradiated diet during gestation (46). In our study, we did not find a correlated trend between PSR value at the center of the injury and behavioral measurements, though the PSR acquisition and analysis methods used here may not be sensitive enough to detect subtle recovery changes at a moderate injury level, or the specific behavioral assessments performed here did not reflect other deficits that may have continued to worsen. Our ongoing studies of SCI in monkeys, however, detected robust demyelination in rostral and caudal spinal segments to the injury center (24). The myelination state of those spared but injury-affected spinal tissue may be a more sensitive indicator of the recovery. The spatial extent and dynamic of the demyelination along the cord after contusion injury needs further investigation.

Sensitivity of PSR and qMT, and DTI parameters in monitoring demyelination

Different MRI parameters are sensitive to different tissue properties, and their combinations can provide additional information to decipher the specific changes in spinal white matter post-SCI. PSR is sensitive to myelin content, but radial and axial diffusivities have also previously been indicated as potential *in vivo* biomarkers of demyelination and axonal damage respectively (31,47,48). In particular, increases in radial diffusivity have been associated with decreases in myelin content, while axonal damage has been correlated with

diminished axial diffusivity. As PSR and radial diffusivity have both been shown to be sensitive to myelin content, a greater correlation was observed between PSR and radial diffusivity than with axial diffusivity as expected. ADC values encompass diffusivity both along and perpendicular to axons, and have been shown to reflect axon size and possibly the thickness of the myelin sheath. The negative but insignificant correlation with PSR may correspond to a decrease in myelin and cell density but also a reduced sensitivity to SCI relative to other metrics. In the context of SCIs, however, the changes observed in radial diffusivity also may not be directly related to demyelination because inflammation may be another confounding factor (further discussed in *Limitations of the Current Study and Future Directions*). With only two b-values and 12 diffusion directions in our acquisition, diffusion metrics here are unable to separate signals originating from intracellular and extracellular diffusion. Along the same lines, ADC values may not be specific enough to reflect axon size and myelin sheath thickness.

Additionally, other parameters derived from the model of MT effects correlated with PSR values. Consistent with our previous SCI study (24), we found positive correlations of PSR with R_{2A} and RM_{0b} and a negative correlation with R_{2b}. The concentration of macromolecules, especially proteins, generally affects relaxation rates, and thus a decrease in R_{2a} with decreased PSR is expected, though this relationship may be dominated by changes in other solutes (proteins) other than myelin which also contribute to PSR. R_{2b}, on the other hand, is more stable across conditions (49), but has also been reported to be sensitive to white matter fiber orientation (50).

Similarly in a recent study, ADC also did not show significant changes at acute phases of SCI that were reflected in FA measurements (10). In both our previous study (24) of a dorsal column lesion model in monkeys and in this study, a high correspondence between FA and PSR was observed. Various factors including axonal density, fiber coherence and myelination can contribute to FA. While correlations between PSR and FA have been less apparent in the brain (51) possibly due to orientation dispersions, the ordered and unidirectional microstructure of the spinal could explain the highly coupled trends between the two observed metrics.

Spinal rsFC as a functional biomarker of the integrity of intraspinal circuit

Spinal cord rsfMRI has only recently been deployed successfully, and to our knowledge there have been only two publications to date that have examined the use of rsFC as a surrogate functional biomarker in pathological conditions: in a NHP dorsal column lesion (20) and human multiple sclerosis patients (52). Similar to our findings here, the introduction of a dorsal column lesion in NHPs induced a reduction in inter-horn correlation values (reduced rsFC) below the injury site (20). In multiple sclerosis patients, functional networks in the spinal cord appear to be intact at 7T although local alterations of connectivity patterns were observed (52). Specifically, dorsal-dorsal and ventral-ventral connectivities were reduced both above and below lesions although no statistical differences were observed in average connectivity or power of low frequency fluctuations in patients compared to controls. Similarly, we found that connectivities between dorsal horns undergo subtle decreases after a contusion injury but with no statistical differences. While direct

comparisons between these studies may not be appropriate due to variations in species and injury models, findings from these studies suggest the presence of reduced connectivity strengths to some degree between horns after a disruption to the cord.

Limitations of the Current Study and Future Directions

The degree of demyelination after SCI is dependent on the type as well as the severity of the injury inflicted. While we have observed a progressive decrease in single PSR measurements at the epicenter over two weeks of monitoring, which was verified with histology, the sensitivity of qMT to tissue changes in different SCI models and over larger volumes of the cord still warrant further investigation. In particular, knowing the extent to which qMT is capable of predicting different grades of injuries to white matter tracts would provide further insights into its potential role as a useful biomarker for particular behaviors or functions. Longitudinal myelin changes at chronic stages as well as whether qMT is able to pick up subtle re-myelination changes produced by therapies are further questions of interest. In this study, a contusion model was selected due to its clinical relevance and to enable comparisons with other models. However, in order to answer some of the above questions, a more controlled injury that produces precise disruption of white matter tracts, such as a tract-targeted transection injury, may be more suitable in evaluating its novel application in SCIs. Moreover, control animals in this study were scanned at one time point. While we do not expect significant variations across a two-week time span that would alter our conclusions, it would be useful to evaluate the variability of quantitative MRI metrics.

Edema, hemorrhage, and inflammation may all occur during acute and subacute phases following a contusion injury, and can confound interpretations of PSR and FA as biomarkers of changes in myelination. In order to control such effects, multi-tensor modelling of additional diffusion signals may be able to resolve different pathologies that are involved (53). At the molecular level, reduced intra-axonal water diffusivity along with infiltrating cells may result in dissociation of their coupled relationship. Moreover, the presence of inflammation has also been shown to affect qMT measurements due to the increase of extra-myelin water protons and pH changes. Notably in rat sciatic nerve *in vitro* experiments, Stanisz et al. found that PSR may not be a robust indicator of myelination in the presence of inflammation two days after tumor necrosis factor-alpha injection (54), while Odrobina et al. noted the difficulty of separating inflammatory effects from demyelination by qMT up to seven days after tellurium diet was provided to weanling rats (55).

We recognize that findings from our rsfMRI studies are still preliminary and fall short in sample sizes at different time points, compared to qMT and DTI measures we were able to obtain from SCI rats. One major issue we encountered during fMRI data acquisition was the hemorrhage which occurred inside the cord and the epidural space (inside CSF) at early stages following a contusion injury. The presence of blood products in and around the spinal cord compromise shimming and cause regional signal drops. These issues led to more variable fMRI signals. While we observed a subtle trend of impaired and subsequent recovered functional connectivity, particularly in the dorsal horns, the small sample size reduces the statistical significances between different stages of the injury. One possible solution is the administration of reversible neuromuscular blockers during fMRI sessions. As

Chen et al. have previously demonstrated in NHPs, functional connectivity recovered over time (20) and it would be valuable to more reliably evaluate whether such a trend is evident in rodents. Additionally, validation of rsfMRI findings reported here with electrophysiology will also be significant for evaluating to what extent neural activity is reflected in the BOLD signal.

Taken together, this is the first study to our knowledge to have applied multi-parametric MRI methods along with behavioral and histological assessments for monitoring of a lumbar contusion SCI rat model. Moreover, technical developments and translations of baseline qMT at the lumbar level are also novel and will inform future studies of organization of the cord under different conditions. Overall, the use of non-invasive multi-parametric MRI allows for examining and monitoring spontaneous changes in microstructure of the injured spinal cord in comprehensive detail. The combination of longitudinal *in vivo* qMT, fMRI and DTI imaging along with behavioral and histological assessments provide complementary information about the pathophysiological basis of the progression and recovery from SCIs.

Supplementary Material

Refer to Web version on PubMed Central for supplementary material.

Acknowledgements

This study is supported by NIH grant NS092961. The author gratefully acknowledges Dr. Zou Yue and Chaohui Tang for their assistance with surgical procedures and perfusion of animals, as well as Frances Shook from the Translational Pathology Shared Resource lab for her help with histology.

Abbreviations

AD	Axial diffusivity
ADC	Apparent diffusion coefficient
BOLD	Blood oxygenation level dependent
CSF	Cerebrospinal fluid
DTI	Diffusion Tensor Imaging
FA	Fractional anisotropy
FDR	False discovery rate
LFB	Luxol fast blue
MRI	Magnetic Resonance Imaging
MTC	Magnetization transfer contrast
NEX	number of excitations
PSR	Pool sized ratio

qMT	Quantitative magnetization transfer
RD	Radial diffusivity
rsFC	Resting state functional connectivity
rsfMRI	Resting state functional MRI
SCI	Spinal cord injury

References

1. Ju G, Wang J, Wang Y & Zhao X. Spinal cord contusion. Neural Regeneration Research 9, 789–794 (2014). [PubMed: 25206890]
2. Fawcett JW & Asher RA The glial scar and central nervous system repair. Brain Research Bulletin 49, 377–391 (1999). [PubMed: 10483914]
3. Casha S, Yu WR & Fehlings MG Oligodendroglial apoptosis occurs along degenerating axons and is associated with FAS and p75 expression following spinal cord injury in the rat. Neuroscience 103, 203–218 (2001). [PubMed: 11311801]
4. Kim DH, Vaccaro AR, Henderson FC & Benzel EC Molecular biology of cervical myelopathy and spinal cord injury: role of oligodendrocyte apoptosis. Spine Journal 3, 510–519 (2003). [PubMed: 14609697]
5. Chan CCM Inflammation: beneficial or detrimental after spinal cord injury? Recent Patents on CNS Drug Discovery 3, 189–199 (2008). [PubMed: 18991808]
6. Hawthorne AL & Popovich PG Emerging concepts in myeloid cell biology after spinal cord injury. Neurotherapeutics 8, (2011).
7. Stejskal EO & Tanner JE Spin diffusion measurements: Spin echoes in the presence of a time-dependent field gradient. The Journal of Chemical Physics 42, 288–292 (1965).
8. Horsfield MA & Jones DK Applications of diffusion-weighted and diffusion tensor MRI to white matter diseases - A review. NMR in Biomedicine 15, 570–577 (2002). [PubMed: 12489103]
9. Vedantam A et al. Diffusion tensor imaging of the spinal cord: Insights from animal and human studies. Neurosurgery 74, 1–8 (2014). [PubMed: 24064483]
10. Li X-H et al. Timing of diffusion tensor imaging in the acute spinal cord injury of rats. Scientific Reports 5, 12639 (2015). [PubMed: 26220756]
11. Loy DN et al. Diffusion tensor imaging predicts hyperacute spinal cord injury severity. Journal of Neurotrauma 24, 979–990 (2007). [PubMed: 17600514]
12. Wolff SD & Balaban RS Magnetization transfer contrast (MTC) and tissue water proton relaxation in vivo. Magnetic Resonance in Medicine (1989).
13. Schmierer K, Scaravilli F, Altmann DR, Barker GJ & Miller DH Magnetization transfer ratio and myelin in postmortem multiple sclerosis brain. Annals of Neurology (2004).
14. Deloire-Grassin MS et al. In vivo evaluation of remyelination in rat brain by magnetization transfer imaging. Journal of the Neurological Sciences 178, 10–6 (2000). [PubMed: 11018243]
15. Henkelman RM et al. Quantitative interpretation of magnetization transfer. Magnetic Resonance in Medicine (1993). doi:10.1002/mrm.1910290607
16. Gochberg DF & Gore JC Quantitative imaging of magnetization transfer using an inversion recovery sequence. Magnetic Resonance in Medicine 49, 501–505 (2003). [PubMed: 12594753]
17. Gore JC Principles and practice of functional MRI of the human brain. Journal of Clinical Investigation 112, 4–9 (2003). [PubMed: 12840051]
18. van den Heuvel MP & Hulshoff Pol HE Exploring the brain network: A review on resting-state fMRI functional connectivity. European Neuropsychopharmacology 20, 519–534 (2010). [PubMed: 20471808]
19. Barry RL, Smith SA, Dula AN & Gore JC Resting state functional connectivity in the human spinal cord. Elife 2014, 1–15 (2014).

20. Chen LM, Mishra A, Yang P-F, Wang F & Gore JC Injury alters intrinsic functional connectivity within the primate spinal cord. Proceedings of the National Academy of Sciences 112, 5991–6 (2015).
21. Wu TL et al. Resting-state functional connectivity in the rat cervical spinal cord at 9.4 T. Magnetic Resonance in Medicine (2018). doi:10.1002/mrm.26905
22. Attwell CL, van Zwieten M, Verhaagen J & Mason MRJ The dorsal column lesion model of spinal cord injury and its use in deciphering the neuron-intrinsic injury response. Developmental Neurobiology (2018).
23. Wang F et al. Multiparametric MRI reveals dynamic changes in molecular signatures of injured spinal cord in monkeys. Magnetic Resonance in Medicine (2014).
24. Wang F et al. Longitudinal assessment of spinal cord injuries in nonhuman primates with quantitative magnetization transfer. Magnetic Resonance in Medicine 1696, 1685–1696 (2015).
25. Cercignani M & Alexander DC Optimal acquisition schemes for in vivo quantitative magnetization transfer MRI. Magnetic Resonance in Medicine 56, 803–810 (2006). [PubMed: 16902982]
26. Ramani A, Dalton C, Miller DH, Tofts PS & Barker GJ Precise estimate of fundamental in-vivo MT parameters in human brain in clinically feasible times. Magnetic Resonance in Medicine (2002).
27. Ramani A, Dalton C, Miller DH, Tofts PS & Barker GJ Precise estimate of fundamental in-vivo MT parameters in human brain in clinically feasible times. Magnetic Resonance in Medicine 20, 721–731 (2002).
28. Henkelman RM et al. Quantitative interpretation of magnetization transfer. Magnetic Resonance in Medicine 29, 759–766 (1993). [PubMed: 8350718]
29. Sled JG & Pike GB Quantitative Interpretation of Magnetization Transfer in Spoiled Gradient Echo MRI Sequences. Journal of Magnetic Resonance (2000).
30. Yang P-F, Wang F & Chen LM Differential fMRI activation patterns to noxious heat and tactile stimuli in the primate spinal cord. Journal of Neuroscience 35, 10493–10502 (2015). [PubMed: 26203144]
31. Janve VA et al. The radial diffusivity and magnetization transfer pool size ratio are sensitive markers for demyelination in a rat model of type III multiple sclerosis (MS) lesions. Neuroimage 74, 298–305 (2013). [PubMed: 23481461]
32. Deuis JR, Dvorakova LS & Vetter I. Methods used to evaluate pain behaviors in rodents. Frontiers in Molecular Neuroscience (2017).
33. Cercignani M & Barker GJ A comparison between equations describing in vivo MT: The effects of noise and sequence parameters. Journal of Magnetic Resonance 191, 171–183 (2008). [PubMed: 18191599]
34. Blight AR Delayed demyelination and macrophage invasion: a candidate for secondary cell damage in spinal cord injury. Central Nervous System Trauma 2, 299–315 (1985). [PubMed: 3836014]
35. Powers BE et al. Axonal thinning and extensive remyelination without chronic demyelination in spinal injured rats. Journal of Neuroscience 32, 5120–5125 (2012). [PubMed: 22496557]
36. Totoiu MO & Keirstead HS Spinal cord injury is accompanied by chronic progressive demyelination. Journal of Comparative Neurology 486, 373–383 (2005). [PubMed: 15846782]
37. Guest JD, Hiester ED & Bunge RP Demyelination and Schwann cell responses adjacent to injury epicenter cavities following chronic human spinal cord injury. Experimental Neurology 192, 384–393 (2005). [PubMed: 15755556]
38. Norenberg MD, Smith J & Marcillo A. The Pathology of Human Spinal Cord Injury: Defining the Problems. Journal of Neurotrauma 21, (2004).
39. Bunge RP, Puckett W & Hiester ED Observations on the pathology of several types of human spinal cord injury, with emphasis on the astrocyte response to penetrating injuries. Advances in neurology 72, 305–315 (1997). [PubMed: 8993707]
40. Plemel JR et al. Remyelination after spinal cord injury: Is it a target for repair? Progress in Neurobiology 117, 54–72 (2014). [PubMed: 24582777]
41. Gledhill RF, Harrison BM & McDonald WI Demyelination and remyelination after acute spinal cord compression. Experimental Neurology 38, 472–487 (1973). [PubMed: 4696114]

42. Ek CJ et al. Pathological changes in the white matter after spinal contusion injury in the rat. PLOS One 7, (2012).
43. Sellers DL, Maris DO & Horner PJ Postinjury niches induce temporal shifts in progenitor fates to direct lesion repair after spinal cord injury. Journal of Neuroscience 29, 6722–6733 (2009). [PubMed: 19458241]
44. Tripathi R & McTigue DM Prominent oligodendrocyte genesis along the border of spinal contusion lesions. Glia 55, 698–711 (2007). [PubMed: 17330874]
45. Plemel JR et al. Remyelination after spinal cord injury: Is it a target for repair? Progress in Neurobiology (2014). doi:10.1016/j.pneurobio.2014.02.006
46. Duncan ID, Brower A, Kondo Y, Curlee JF & Schultz RD Extensive remyelination of the CNS leads to functional recovery. Proceedings of the National Academy of Sciences 106, 6832–6836 (2009).
47. Song SK et al. Demyelination increases radial diffusivity in corpus callosum of mouse brain. Neuroimage 26, 132–140 (2005). [PubMed: 15862213]
48. Ou X & Gochberg DF MT effects and T1 quantification in single-slice spoiled gradient echo imaging. Magnetic Resonance in Medicine 59, 835–845 (2008). [PubMed: 18302249]
49. Smith S a et al. Quantitative magnetization transfer characteristics of the human cervical spinal cord in vivo: application to adrenomyeloneuropathy. Magnetic Resonance in Medicine 61, 22–7 (2009). [PubMed: 19097204]
50. Cercignani M, Dowell NG & Tofts PS Quantitative MRI of the Brain: Principles of Physical Measurement, Second edition (Series in Medical Physics and Biomedical Engineering) 2nd Edition (CRC Press, 2018).
51. Underhill H, Yuan C & Yarnykh V Direct quantitative comparison between cross-relaxation imaging and diffusion tensor imaging of the human brain. Proceedings 17th Scientific Meeting, International Society for Magnetic Resonance in Medicine, 2749 (2009).
52. Conrad BN et al. Multiple sclerosis lesions affect intrinsic functional connectivity of the spinal cord. Brain (2018).
53. Wang Y et al. Differentiation and quantification of inflammation, demyelination and axon injury or loss in multiple sclerosis. Brain (2015).
54. Stanisz GJ, Webb S, Munro C, Pun T & Midha R. MR properties of excised neural tissue following experimentally induced inflammation. Magnetic Resonance in Medicine 51, 473–479 (2004). [PubMed: 15004787]
55. Odrobina EE, Lam TYJ, Pun T, Midha R & Stanisz GJ MR properties of excised neural tissue following experimentally induced demyelination. NMR in Biomedicine 18, 277–284 (2005). [PubMed: 15948233]

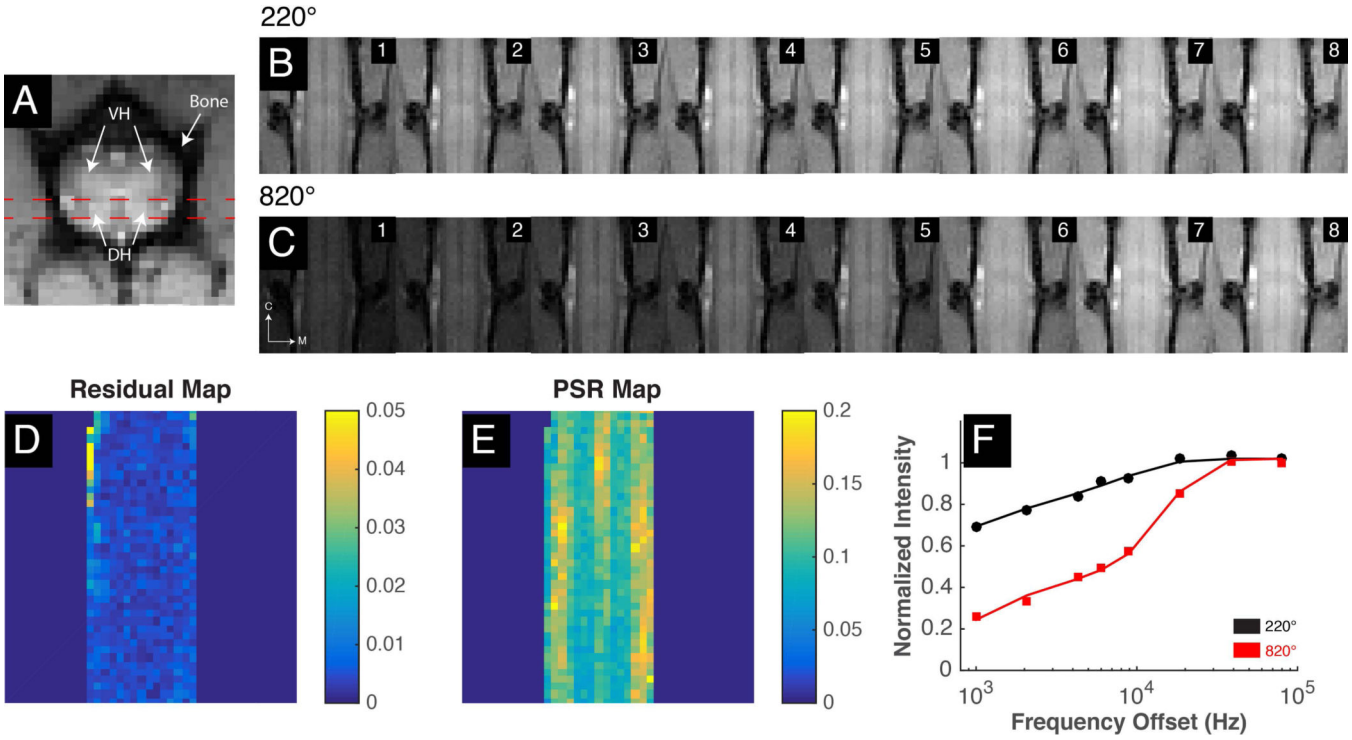

Figure 1: QMT acquisition and analysis for healthy lumbar spinal cord.

(A) High resolution axial MTC image with red dashed lines indicating coronal acquisition plan covering dorsal horns and the dorsal column. (B-C) Cropped raw qMT data collected at eight different frequency offsets and at two flip angles of 220° and 820° respectively. M: medial; C: caudal. (D-E) Square 2-norm of residuals and PSR map from qMT model fitting. (F) Curves of normalized intensity in selected white matter voxel with fitted model curves for 220° and 820° represented as black and red colors respectively. Doral horns, DH; Ventral horns, VH.

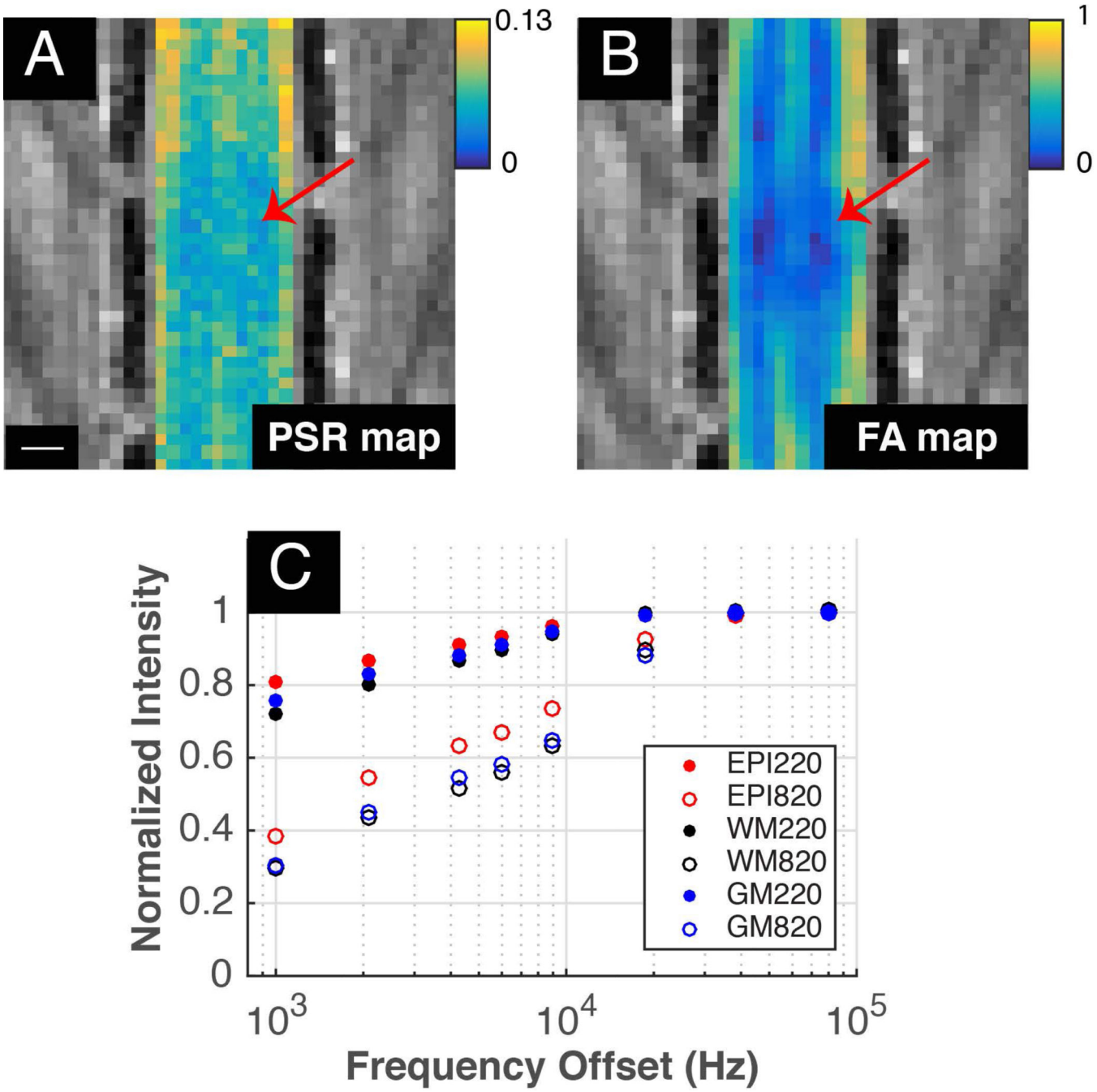

Figure 2: PSR and FA maps with MT curve post-SCI.

(A) PSR and (B) FA maps 24 hours post-SCI. Red arrows indicate epicenter of the injury while scale bar represents 1mm. (C) ROIs were drawn at the epicenter (red) as well as at gray (blue) and white (black) matter at least 5mm away from the epicenter. MT spectra of these ROIs at flip angles 220° (filled) and 820° (unfilled) are displayed.

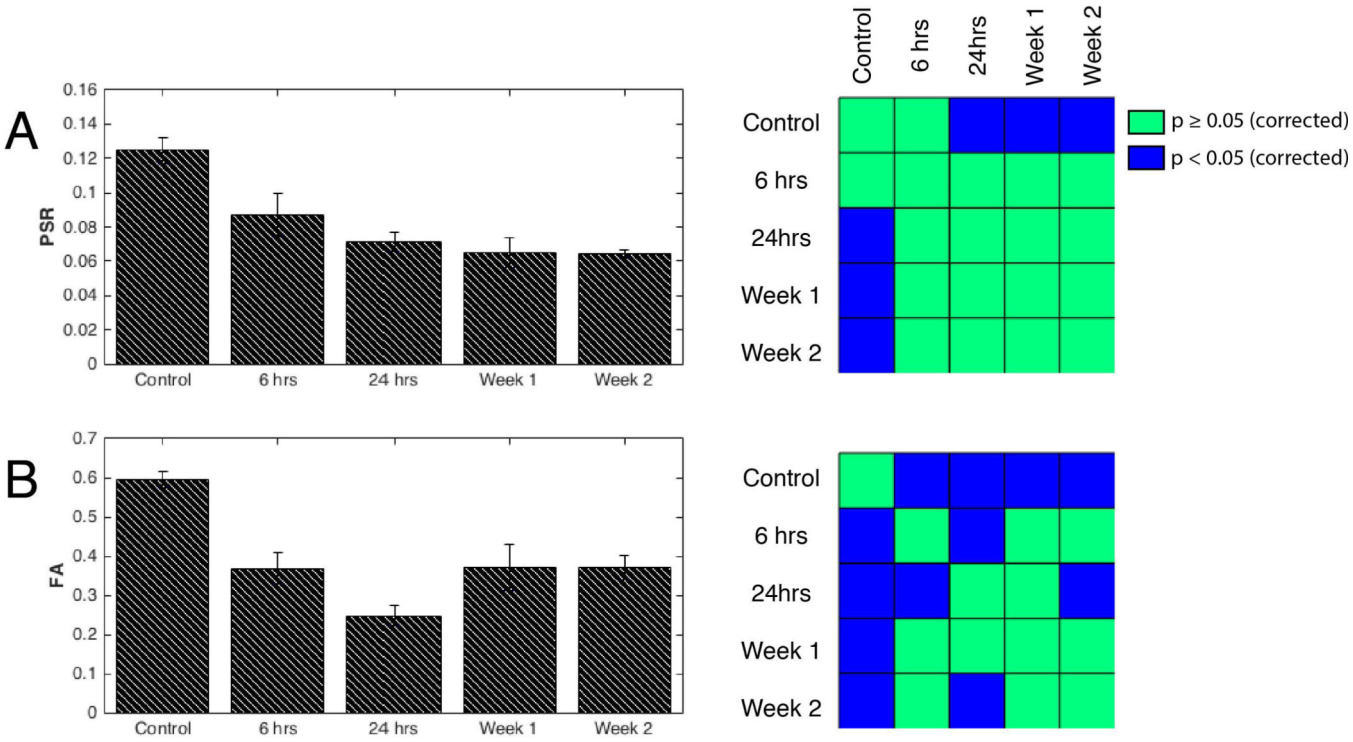

Figure 3: Longitudinal assessments of the injury.

(A, left) Averaged PSR values for controls and different time points of the injury at 6 hours, 24 hours, week 1 and week 2 with n=6, 7, 11, 8, 5 observations respectively. (A, right) Non-parametric Wilcoxon rank sum tests between different time points of the injury. Blue and green voxels represent FDR corrected p-values greater than or equal to 0.05 and less than 0.05 respectively. Likewise, (B, left) averaged FA values along with (B, right) statistical comparisons were computed from runs at different time points of the injury from the same animals. n=6, 7, 10, 8, 5 observations for 6 hours, 24 hours, week 1 and week 2 respectively; DTI was not acquired for one run at the week-1 time point.

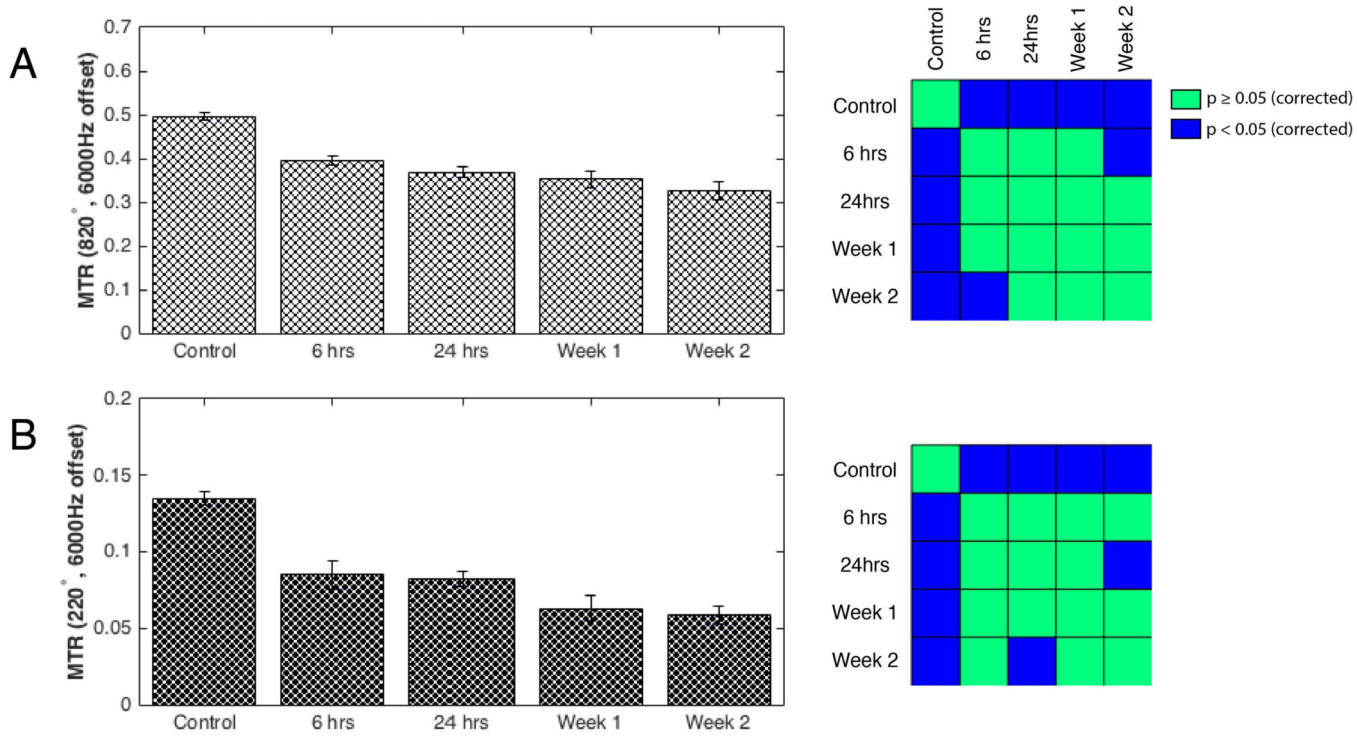

Figure 4: Conventional 2-point Magnetization Transfer Ratio (MTR) measurements.

Semi-quantitative MTR quantifications were made using data from RF offset at 6000Hz and 80000Hz for saturation flip angles of 820° (A, left) and 220° (B, left). Diminishing trends of MTR are revealed for both saturation flip angles which is consistent with qMT PSR measurements. Pearson's correlation with PSR longitudinal measurements in Figure 3 are 0.99 (p=0.002) and 0.98 (p=0.003) for flip angles 820° and 220° respectively. Non-parametric Wilcoxon rank sum tests between different time points of the injury for saturation flip angles of 820° (A, right) and 220° (B, right). Blue and green voxels represent FDR corrected p-values greater than or equal to 0.05 and less than 0.05 respectively.

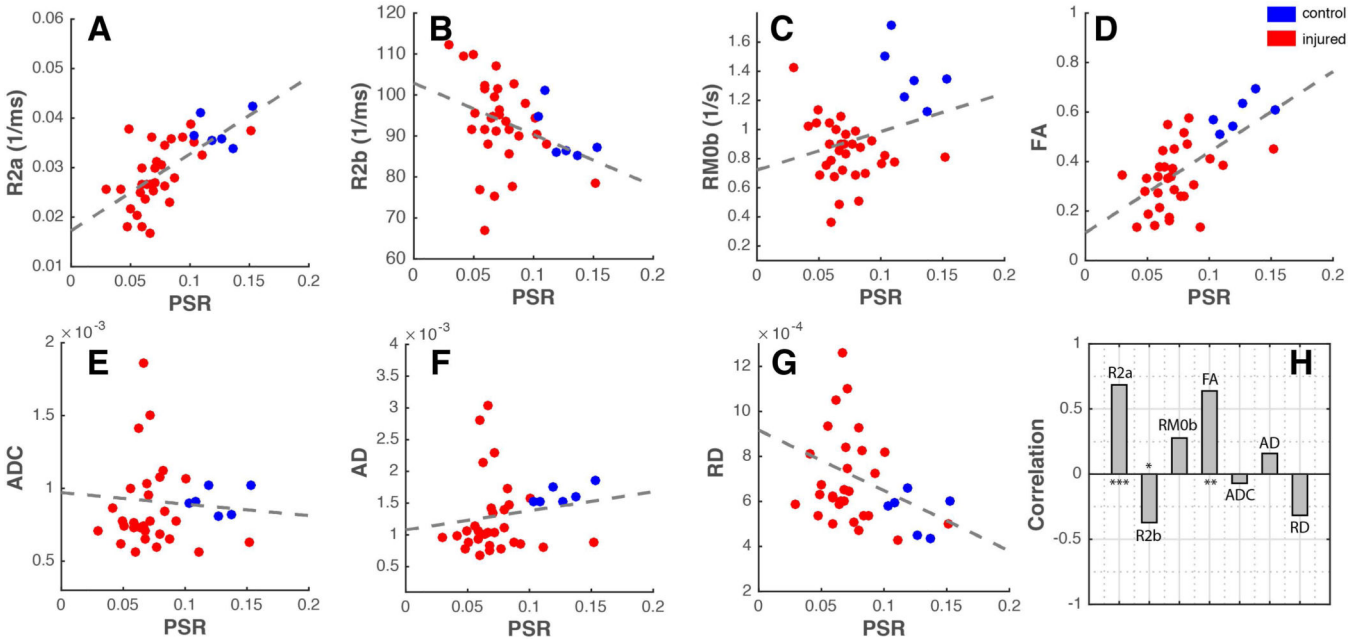

Figure 5: Comparisons of PSR and other MRI parameters.

(A-G) Plots of R_{2a}, R_{2b}, RM_{0b}, FA, ADC, AD and RD as a function of PSR. Dotted lines indicate linear fits for each plot while blue and red dots represent averaged metric measured for control and SCI animals respectively. (H) Correlation between PSR and respective MRI parameters at all time points for both control and SCI animals. ***$p<0.000005$, **$p<0.00005$, and *$p<0.05$.

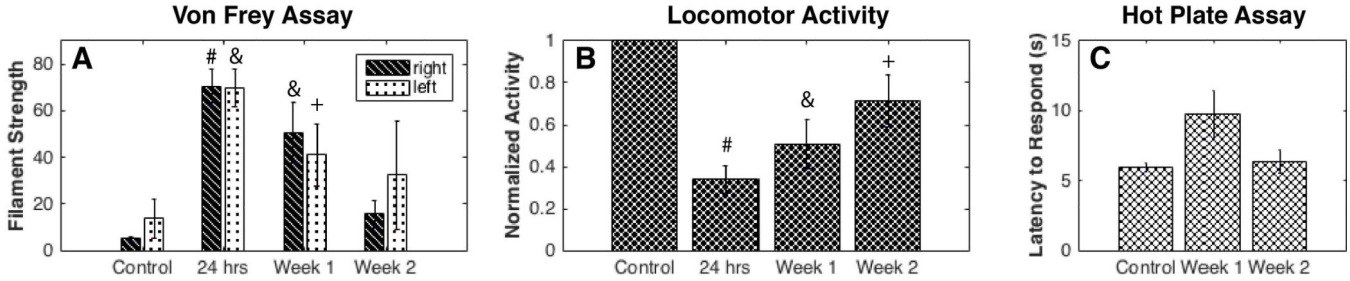

Figure 6: Behavioral assessments post-SCI.

(A) Threshold filament forces that caused positive responses through either withdrawing or licking with the Von Frey test are displayed at different time points post-SCI. (B) Normalized locomotor activity assessed with the number of beam breaks in an open field chamber. Non-parametric Wilcoxon-rank sum tests were performed relative to their respective baselines. (C) Latencies to respond to a 55 degrees Celsius hot plate were recorded. Non-parametric Wilcoxon-rank sum tests were performed relative to their respective baselines. $^{\#}p<0.0005$, $^{\&}p<0.005$, and $^{+}p<0.05$.

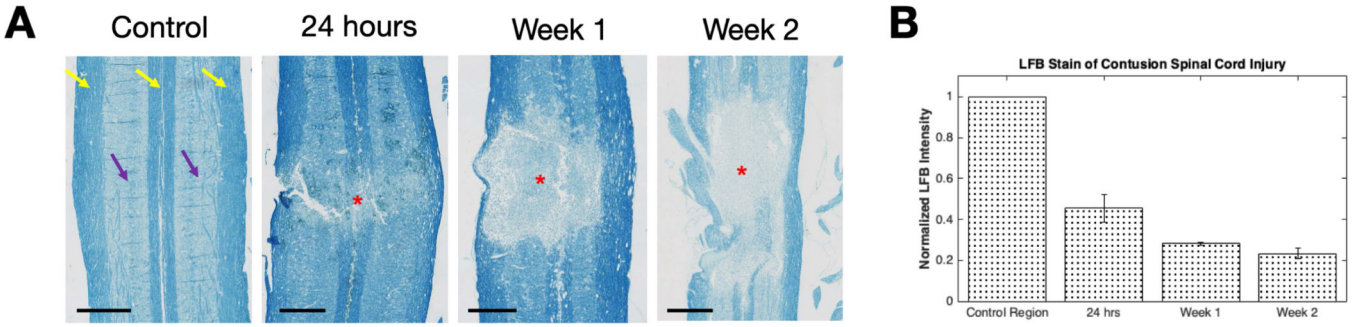

Figure 7: LFB stains of the spinal cord at different time points post SCI.

(A) Controls, 24-hours, Week-1 and Week-2 time points of the spinal cord were stained for myelin using Luxol Fast Blue. Purple and yellow arrows point to gray and white matter regions that are indicated by weaker and more intense stains respectively. Red asterisks indicate epicenter of the injury with de-myelination are present while scale bars represent 1mm. (B) Histogram of normalized LFB intensity of the injury site relative to control regions unaffected by the injury in each animal.

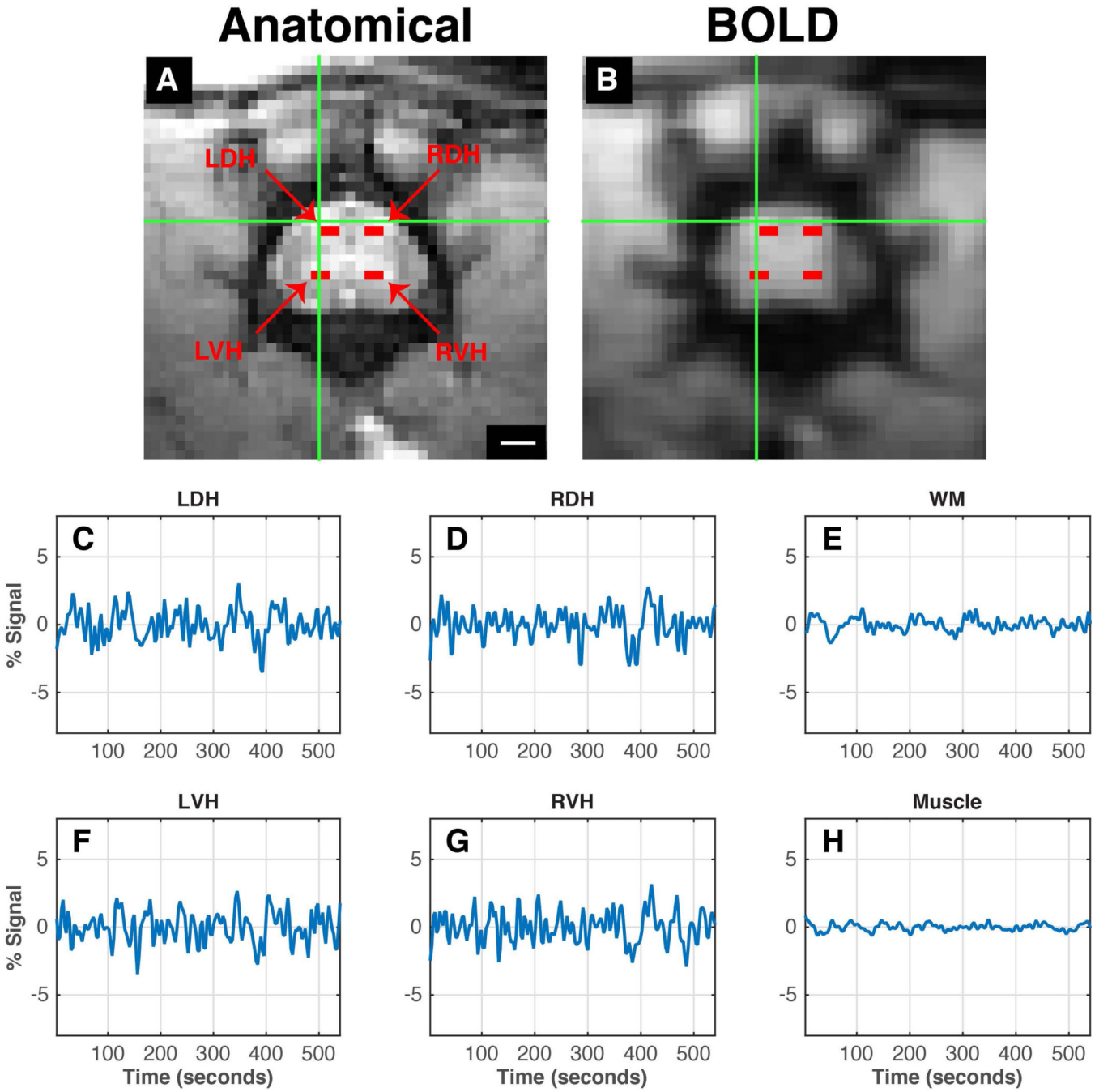

Figure 8: Anatomical and functional images of the lumbar spinal cord.

(A) Enlarged views of the lumbar spinal cord with magnetization transfer contrast; scale bar represents 1mm. (B) Pre-processed functional BOLD image of the same imaging plane. Goodness of alignment between the anatomical and functional image is indicated by the green crosshair pointing to the left dorsal horn. Horns of the lumbar spinal cord are indicated as red voxels – left dorsal horn, LDH; left ventral horn, LVH; right dorsal horn, RDH; right ventral horn, RVH. (C-H) Averaged time series of the selected voxels of the corresponding horns of the spinal cord, white matter and muscle.

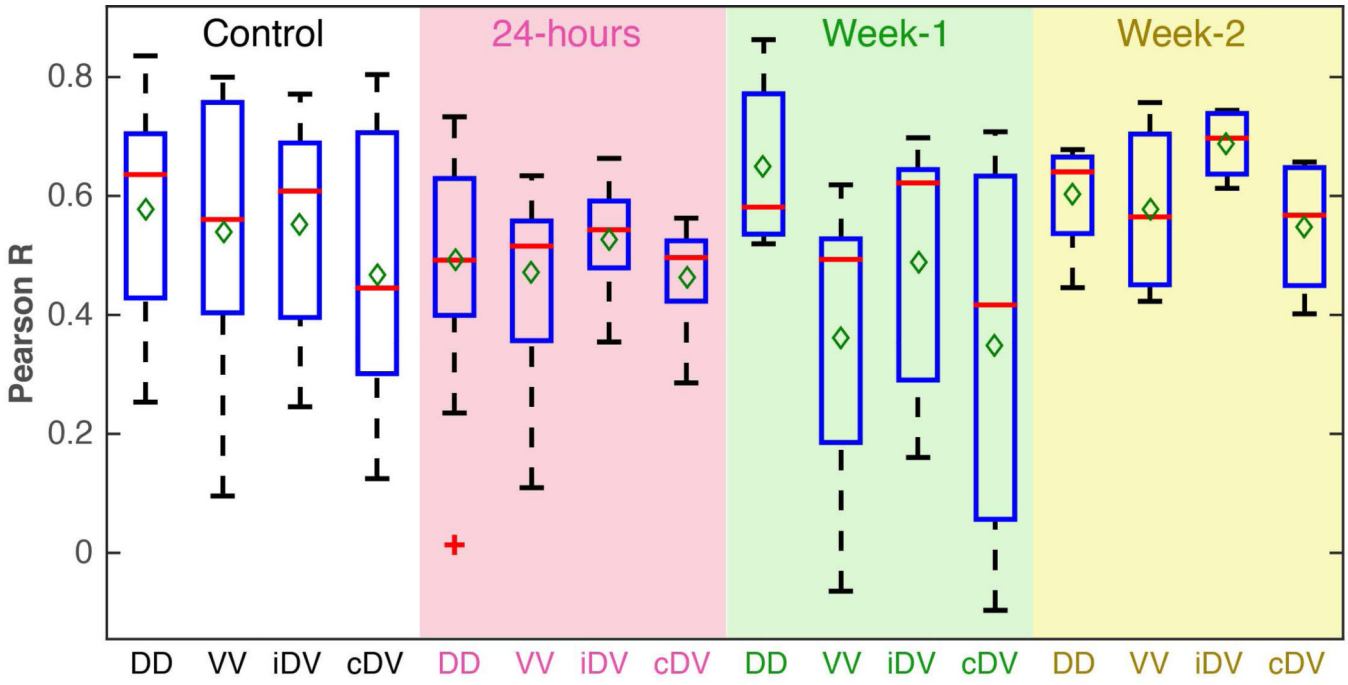

Figure 9: Longitudinal functional connectivity changes post-SCI below the injury site.

Boxplots between each spinal horn in controls (white background), 24-hours (pink background), Week-1 (green background) and Week-2 (yellow background) post-injury. Boxplots at each timepoint contains 14 runs (four animals), 21 runs (five animals), 5 runs (two animals) and 4 runs (one animal) for controls, 24-hours, Week-1 and Week-2 respectively. Red lines and green diamonds represent medians and means of each boxplot respectively. Dorsal-dorsal horn connectivity, DD; Ventral-ventral horn connectivity, VV; ipsilateral dorsal-ventral horn connectivity, iDV; contralateral dorsal-ventral horn connectivity.